

Metin Muradoglu¹

Department of Mechanical Engineering,
Koc University,
Rumelifeneri Yolu,
Sariyer, Istanbul 34450, Turkey
e-mail: mmuradoglu@ku.edu.tr

Seckin Gokaltun²

Computational Science and Engineering
Program,
Informatics Institute,
Istanbul Technical University,
Maslak, Sariyer, Istanbul 34469, Turkey
e-mail: gokaltunse@itu.edu.tr

Implicit Multigrid Computations of Buoyant Drops Through Sinusoidal Constrictions

Two-dimensional computations of dispersed multiphase flows involving complex geometries are presented. The numerical algorithm is based on the front-tracking method in which one set of governing equations is written for the whole computational domain and different phases are treated as a single fluid with variable material properties. The front-tracking methodology is combined with a newly developed finite volume solver based on dual time-stepping, diagonalized alternating direction implicit multigrid method. The method is first validated for a freely rising drop in a straight channel, and it is then used to compute a freely rising drop in various constricted channels. Interaction of two buoyancy-driven drops in a continuously constricted channel is also presented.

[DOI: 10.1115/1.1795222]

1 Introduction

Dynamics of dispersed bubbles or drops in capillary flows involving complex geometries has attracted considerable interest due to its applications in enhanced oil recovery, hazardous waste management, microfluidic devices, and biological systems [1–3].

The presence of deforming phases makes the multiphase flow computations a challenging task, and strong interactions between the phases and complex geometries add further complexity to the problem. Therefore, the progress was rather slow and the computations of multiphase flows have been usually restricted to simple geometries [4] or to moderately complex geometries in the limiting case of creeping flow regime [5,6]. Since nearly all-multiphase flows of practical importance involve complex geometries, it is of obvious interest to extend the modeling and computational techniques to treat multiphase flows in arbitrarily complex geometries.

The motion of a drop in a constricted capillary tube has been studied experimentally by Olbricht and Leal [1], Olbricht and Kung [7], and Hemmat and Borhan [2], and computationally in the creeping flow regime by Tsai and Miksis [5] and Magna [6]. Udaykumar et al. [3] performed computations of the motion of droplets in a constricted channel at finite Reynolds numbers by using a mixed Eulerian-Lagrangian method.

In the present work, a finite-volume/front-tracking (FV/FT) method is used to simulate dynamics of two-dimensional drops rising due to buoyancy in various constricted channels. The front-tracking (FT) method developed by Unverdi and Tryggvason [8] is incorporated into a newly developed finite-volume (FV) algorithm in order to facilitate efficient and accurate simulations of dispersed multiphase flows in arbitrarily complex geometries. The front-tracking method is based on writing one set of governing equations for the whole computational domain and treating different phases as a single fluid with variable material properties. In this method, the fronts are explicitly tracked in a Lagrangian frame and the effects of surface tension are accounted for by

treating them as body forces. The front tracking method has been successfully applied to a variety of dispersed multiphase flow problems, but all in relatively simple geometries. A detailed description of the front-tracking method can be found in the review paper by Tryggvason et al. [4]. The FV method used in the present work is based on the concept of the dual (or pseudo) time-stepping method and is developed for unsteady computations of incompressible laminar flows. The dual time-stepping method uses subiterations in pseudotime and has a number of advantages, such as direct coupling of the continuity and momentum equations in incompressible flow equations, the elimination of factorization error in factored implicit schemes, the elimination of errors due to approximations made in the implicit operator to improve numerical efficiency, the elimination of errors due to lagged boundary conditions at both solid and internal fluid boundaries, and the ability to use nonphysical, preconditioned iterative methods for more efficient convergence of the subiterations as discussed by Caughey [9]. In order to combine the front-tracking methodology with the FV method, an algorithm is developed for tracking the front in curvilinear grids and is found to be very efficient and robust. The details of the present FV/FT method can be found in Muradoglu and Kayaalp [10].

The paper begins with a brief description of the governing equations and the numerical solution algorithm. The results are then presented and discussed in Section 4. The present FV/FT method is first validated for a freely rising drop in a straight channel, and the results are compared with the results of the finite-difference/front-tracking (FD/FT) method implemented in the FTC2D code of Unverdi and Tryggvason [8]. It is then applied to a single drop rising in various constricted channels. Interactions of two identical drops are also studied in the continuously constricted channel. Finally, some conclusions are drawn in Section 5.

¹To whom correspondence should be addressed.

²Present address: Department of Mechanical Engineering, Florida International University, EAS 2417, 10855 W. Flagler Street, Miami, FL 33174.

Contributed by the Applied Mechanics Division of THE AMERICAN SOCIETY OF MECHANICAL ENGINEERS for publication in the ASME JOURNAL OF APPLIED MECHANICS. Manuscript received by the Applied Mechanics Division, August 25, 2003; final revision; June 17, 2004. Associate Editor: T. E. Tezduyar. Discussion on the paper should be addressed to the Editor, Prof. Robert M. McMeeking, Journal of Applied Mechanics, Department of Mechanical and Environmental Engineering, University of California—Santa Barbara, Santa Barbara, CA 93106-5070, and will be accepted until four months after final publication of the paper itself in the ASME JOURNAL OF APPLIED MECHANICS.

2 Mathematical Formulation

Following Unverdi and Tryggvason [8], the Navier-Stokes equations are written for the whole flow field, and different phases are treated with variable material properties. The effects of surface tension are modeled as body forces and are included in the momentum equations as δ functions at the phase boundaries. In the

Cartesian coordinates, two-dimensional time-dependent Navier-Stokes equations for incompressible flow can be written in conservative form as

$$\frac{\partial \mathbf{q}}{\partial t} + \frac{\partial \mathbf{f}}{\partial x} + \frac{\partial \mathbf{g}}{\partial y} = \frac{\partial \mathbf{f}_v}{\partial x} + \frac{\partial \mathbf{g}_v}{\partial y} - \Delta \rho \mathbf{G} + \int \delta(\mathbf{x} - \mathbf{x}_f) \sigma \kappa \mathbf{n} ds \quad (1)$$

where

$$\mathbf{q} = \begin{pmatrix} 0 \\ \rho u \\ \rho v \end{pmatrix}, \quad \mathbf{f} = \begin{pmatrix} u \\ p + \rho u^2 \\ \rho uv \end{pmatrix}, \quad \mathbf{g} = \begin{pmatrix} v \\ \rho uv \\ p + \rho v^2 \end{pmatrix},$$

$$\mathbf{f}_v = \begin{pmatrix} 0 \\ \tau_{xx} \\ \tau_{xy} \end{pmatrix}, \quad \mathbf{g}_v = \begin{pmatrix} 0 \\ \tau_{xy} \\ \tau_{yy} \end{pmatrix} \quad (2)$$

and the viscous stresses are given for a Newtonian fluid as

$$\tau_{xx} = 2\mu \frac{\partial u}{\partial x}, \quad \tau_{xy} = \mu \left(\frac{\partial u}{\partial y} + \frac{\partial v}{\partial x} \right), \quad \tau_{yy} = 2\mu \frac{\partial v}{\partial y} \quad (3)$$

In Eqs. (1)–(3), u , v , p , ρ , and μ denote the velocity components in x and y directions, the pressure, the density, and the dynamic viscosity, respectively. The third term on the right-hand side of Eq. (1) represents the body force due to buoyancy with \mathbf{G} being the gravitational acceleration and $\Delta \rho = \rho_o - \rho$, where ρ_o is the density of the ambient fluid. The last term represents the effects of the surface tension and δ , \mathbf{x}_f , σ , κ , \mathbf{n} and ds denote the Dirac delta function, the location of the front, the surface tension coefficient, the curvature, the outward unit normal vector on the interface, and the arc length along the interface, respectively.

The fluids in and out of the drop are assumed to be incompressible, and the effects of heat transfer are neglected. Therefore, the viscosity and the density remain constant in each fluid particle, i.e.,

$$\frac{D\rho}{Dt} = 0, \quad \frac{D\mu}{Dt} = 0 \quad (4)$$

The flow regime of bubbly flows is characterized by four nondimensional parameters as discussed by Clift et al. [11]. These are the Morton number $M = \mu_o^4 (\rho_o - \rho_b) G / \rho_o^2 \sigma^3$, the Eötvös number $Eu = (\rho_o - \rho_b) d_e^2 G / \sigma$, the density ratio $\gamma = \rho_b / \rho_o$, and the viscosity ratio $\zeta = \mu_b / \mu_o$, where d_e is the equivalent drop diameter and the subscripts o and b refer to the ambient and the drop fluids, respectively. The Reynolds number is defined as $Re = \rho_o V d_e / \mu_o$, where V is the rise velocity.

3 Numerical Procedure

As can be seen in Eq. (1), the continuity equation is decoupled from the momentum equations because it does not have any time derivative term in incompressible flows. To circumvent this difficulty and to be able to use time-marching algorithms, pseudotime derivative terms augmented with a preconditioning matrix are added to Eq. (1) yielding

$$\Gamma^{-1} \frac{\partial \mathbf{w}}{\partial \tau} + \frac{\partial \mathbf{q}}{\partial t} + \frac{\partial \mathbf{f}}{\partial x} + \frac{\partial \mathbf{g}}{\partial y} = \frac{\partial \mathbf{f}_v}{\partial x} + \frac{\partial \mathbf{g}_v}{\partial y} - (\rho_o - \rho) \mathbf{G} + \int \delta(\mathbf{x} - \mathbf{x}_f) \sigma \kappa \mathbf{n} ds \quad (5)$$

with

$$\mathbf{w} = \begin{pmatrix} p \\ u \\ v \end{pmatrix}, \quad \Gamma^{-1} = \begin{pmatrix} \frac{1}{\rho \beta^2} & 0 & 0 \\ \frac{2\alpha u}{\beta^2} & \rho & 0 \\ \frac{2\alpha v}{\beta^2} & 0 & \rho \end{pmatrix} \quad (6)$$

where β is a preconditioning parameter with dimensions of velocity and α is a dimensionless parameter to be determined. In Eq. (5), τ denotes the pseudotime and the dual time-stepping method is based on marching in pseudotime until a convergence is reached for each physical time step. Since the transient solution in pseudotime is not of interest, we are free to use any nonphysical convergence acceleration technique, such as preconditioning, local time-stepping, and multigrid methods. To facilitate treatment of complex geometries, Eq. (5) is transformed into a curvilinear coordinates defined by

$$\xi = \xi(x, y), \quad \eta = \eta(x, y) \quad (7)$$

Using the relation $\mathbf{q} = \mathbf{I}^1 \rho \mathbf{w}$ where the incomplete identity matrix \mathbf{I}^1 is defined as

$$\mathbf{I}^1 = \begin{bmatrix} 0 & 0 & 0 \\ 0 & 1 & 0 \\ 0 & 0 & 1 \end{bmatrix} \quad (8)$$

and the transformation given by Eq. (7), the transformed equations in the curvilinear coordinates can be written as

$$\Gamma^{-1} \frac{\partial h \mathbf{w}}{\partial \tau} + \mathbf{I}^1 \frac{\partial h \rho \mathbf{w}}{\partial t} + \frac{\partial h \mathbf{F}}{\partial \xi} + \frac{\partial h \mathbf{G}}{\partial \eta} = \frac{\partial h \mathbf{F}_v}{\partial \xi} + \frac{\partial h \mathbf{G}_v}{\partial \eta} + h \mathbf{f}_b \quad (9)$$

where $h = x_\xi y_\eta - x_\eta y_\xi$ is the determinant of the Jacobian of the transformation and $h \mathbf{F}$, $h \mathbf{G}$, $h \mathbf{F}_v$, and $h \mathbf{G}_v$ are the transformed convective and viscous fluxes given by

$$h \mathbf{F} = y_\eta \mathbf{f} - x_\eta \mathbf{g}, \quad h \mathbf{F}_v = y_\eta \mathbf{f}_v - x_\eta \mathbf{g}_v, \quad (10)$$

$$h \mathbf{G} = -y_\xi \mathbf{f} + x_\xi \mathbf{g}, \quad h \mathbf{G}_v = -y_\xi \mathbf{f}_v + x_\xi \mathbf{g}_v$$

The vector \mathbf{f}_b represents the last two terms on the right-hand side of Eq. (1), namely, the sum of the buoyancy forces and the surface tension. Following Caughey [9], subiterated implicit scheme to solve Eq. (9) can be written as

$$\Gamma^{-1} h \frac{\mathbf{w}^{p+1} - \mathbf{w}^p}{\Delta \tau} + \mathbf{I}^1 \frac{3(\rho h \mathbf{w})^{p+1} - 4(\rho h \mathbf{w})^n + (\rho h \mathbf{w})^{n-1}}{2 \Delta t}$$

$$= \theta \left[\frac{\partial h \mathbf{F}_v}{\partial \xi} + \frac{\partial h \mathbf{G}_v}{\partial \eta} + h \mathbf{f}_b \right]^p - \theta \left[\frac{\partial h \mathbf{F}}{\partial \xi} + \frac{\partial h \mathbf{G}}{\partial \eta} \right]^{p+1} - (1 - \theta)$$

$$\times \left[\frac{\partial h(\mathbf{F} - \mathbf{F}_v)}{\partial \xi} + \frac{\partial h(\mathbf{G} - \mathbf{G}_v)}{\partial \eta} - h \mathbf{f}_b \right]^n \quad (11)$$

where $()^p$ denotes the p th level of the subiteration and $()^n$ denotes the n th level of the physical time step. The iterations in the physical and pseudotimes are called the outer and inner iterations, respectively. The parameter θ is the implicitness factor with $\theta = 1$, corresponding to a fully implicit method in pseudotime. As can be seen in Eq. (11), the viscous and source terms are treated implicitly in the physical time and explicitly in the pseudotime. The correction $\Delta \mathbf{w} = \mathbf{w}^{p+1} - \mathbf{w}^p$ is computed in each subiteration according to

$$\begin{aligned}
h \left(\frac{\Gamma^{-1}}{\Delta \tau} + \frac{3\rho}{2\Delta t} \mathbf{I} \right) \Delta \mathbf{w}^p = & -\mathbf{I} \left[\frac{3(\rho h \mathbf{w})^p - 4(\rho h \mathbf{w})^n + (\rho h \mathbf{w})^{n-1}}{2\Delta t} \right] \\
& + \theta \left[\frac{\partial h \mathbf{F}_v}{\partial \xi} + \frac{\partial h \mathbf{G}_v}{\partial \eta} + h \mathbf{f}_b \right]^p - \theta \left[\frac{\partial h \mathbf{F}}{\partial \xi} \right. \\
& \left. + \frac{\partial h \mathbf{G}}{\partial \eta} \right]^{p+1} - (1-\theta) \left[\frac{\partial h(\mathbf{F} - \mathbf{F}_v)}{\partial \xi} \right. \\
& \left. + \frac{\partial h(\mathbf{G} - \mathbf{G}_v)}{\partial \eta} - h \mathbf{f}_b \right]^n \quad (12)
\end{aligned}$$

As can be seen in Eq. (12), when a steady state is reached in the pseudotime, i.e., $\Delta \mathbf{w}^p = 0$, we have $(\)^p \rightarrow (\)^{n+1}$. Therefore the method is equivalent to the second-order implicit backward Euler method in the physical time. To solve Eq. (12), the convective fluxes are linearized in pseudotime according to

$$\begin{aligned}
\left(\frac{\partial h \mathbf{F}}{\partial \xi} \right)^{p+1} &= \left(\frac{\partial h \mathbf{F}}{\partial \xi} \right)^p + \mathbf{A} \frac{\partial \Delta \mathbf{w}^p}{\partial \xi} + O(\Delta \tau^2) \\
\left(\frac{\partial h \mathbf{G}}{\partial \eta} \right)^{p+1} &= \left(\frac{\partial h \mathbf{G}}{\partial \eta} \right)^p + \mathbf{B} \frac{\partial \Delta \mathbf{w}^p}{\partial \eta} + O(\Delta \tau^2) \quad (13)
\end{aligned}$$

where the Jacobian matrices are defined as

$$\mathbf{A} = \left(\frac{\partial \mathbf{F}}{\partial \mathbf{w}} \right)^p, \quad \mathbf{B} = \left(\frac{\partial \mathbf{G}}{\partial \mathbf{w}} \right)^p \quad (14)$$

From Eqs. (12)–(14), the linearized equations can be written as

$$\left[\mathbf{I} + \frac{\theta \Delta \tau}{h} \left(\tilde{\mathbf{A}} \frac{\partial}{\partial \xi} + \tilde{\mathbf{B}} \frac{\partial}{\partial \eta} \right) \right] \Delta \mathbf{w}^p = \mathbf{R} \quad (15)$$

where the residual vector is defined as

$$\begin{aligned}
\mathbf{R} = & -\mathbf{D}^{-1} \mathbf{I}^1 \frac{\Delta \tau}{\rho h} \left[\frac{3(\rho h \mathbf{w})^p - 4(\rho h \mathbf{w})^n + (\rho h \mathbf{w})^{n-1}}{2\Delta t} \right] \\
& - \frac{\Delta \tau \mathbf{D}^{-1} \Gamma}{h} \left\{ \theta \left[\frac{\partial h(\mathbf{F} - \mathbf{F}_v)}{\partial \xi} + \frac{\partial h(\mathbf{G} - \mathbf{G}_v)}{\partial \eta} - h \mathbf{f}_b \right]^p + (1-\theta) \right. \\
& \left. \times \left[\frac{\partial h(\mathbf{F} - \mathbf{F}_v)}{\partial \xi} + \frac{\partial h(\mathbf{G} - \mathbf{G}_v)}{\partial \eta} - h \mathbf{f}_b \right]^n \right\} \quad (16)
\end{aligned}$$

and

$$\tilde{\mathbf{A}} = \mathbf{D}^{-1} \Gamma \mathbf{A}; \quad \tilde{\mathbf{B}} = \mathbf{D}^{-1} \Gamma \mathbf{B}; \quad \mathbf{D} = \mathbf{I} + \frac{3\Delta \tau}{2\Delta t} \mathbf{I}^1 \quad (17)$$

Following Caughey [9], Eq. (15) is factorized as

$$\left[\mathbf{I} + \frac{\theta \Delta \tau}{h} \tilde{\mathbf{A}} \frac{\partial}{\partial \xi} \right] \left[\mathbf{I} + \frac{\theta \Delta \tau}{h} \tilde{\mathbf{B}} \frac{\partial}{\partial \eta} \right] \Delta \mathbf{w}^p = \mathbf{R} \quad (18)$$

which can be solved efficiently in two steps by using a block tridiagonal solver. However, Eq. (18) can be solved more efficiently using the diagonalization procedure. The diagonalization is possible because the inviscid part of the preconditioned equations are hyperbolic, so there exist modal matrices $\mathbf{Q}_{\tilde{\mathbf{A}}}$ and $\mathbf{Q}_{\tilde{\mathbf{B}}}$ such that

$$\tilde{\mathbf{A}} = \mathbf{Q}_{\tilde{\mathbf{A}}}^{-1} \tilde{\mathbf{A}} \mathbf{Q}_{\tilde{\mathbf{A}}}; \quad \tilde{\mathbf{B}} = \mathbf{Q}_{\tilde{\mathbf{B}}}^{-1} \tilde{\mathbf{B}} \mathbf{Q}_{\tilde{\mathbf{B}}} \quad (19)$$

and the diagonal matrices having real eigenvalues. The diagonalized algorithm is then given by

$$\left[\mathbf{I} + \frac{\theta \Delta \tau}{h} \tilde{\mathbf{A}} \frac{\partial}{\partial \xi} \right] \mathbf{Q}_{\tilde{\mathbf{A}}}^{-1} \mathbf{Q}_{\tilde{\mathbf{B}}} \left[\mathbf{I} + \frac{\theta \Delta \tau}{h} \tilde{\mathbf{B}} \frac{\partial}{\partial \eta} \right] \Delta \mathbf{V}^p = \mathbf{Q}_{\tilde{\mathbf{A}}}^{-1} \mathbf{R} \quad (20)$$

where $\Delta \mathbf{V}^p = \mathbf{Q}_{\tilde{\mathbf{B}}}^{-1} \Delta \mathbf{w}^p$. Equation (20) is solved in two steps using a scalar tridiagonal solver in each step. Note that the spatial derivatives are approximated by a cell-centered finite volume method, which is equivalent to second-order central differences on a regular Cartesian grid and fourth-order numerical dissipation

terms similar to that of Caughey [9] are added explicitly to the right-hand side of Eq. (18) to prevent the odd-even decoupling.

A front-tracking method similar to that of Unverdi and Tryggvason [8] is developed for treatment of the different phases and the surface tension. In this method, the interface is divided into small line segments called front elements, and the end points of each element are tracked explicitly in a Lagrangian frame. The details of the numerical method can be found in Muradoglu and Kayaalp [10]. The complete solution procedure can be summarized as follows:

In advancing solutions from physical time level n ($t_n = n \cdot \Delta t$) to level $n+1$, the locations of front points at the new time level $n+1$ are first predicted using an explicit Euler method, i.e.,

$$\mathbf{X}_f^{n+1} = \mathbf{X}_f^n + \Delta t \mathbf{V}_f^n \quad (21)$$

where \mathbf{X}_f and \mathbf{V}_f denote the position of front points and the flow velocity interpolated from the neighboring fixed grid points onto front point \mathbf{X}_f , respectively. Then the material properties and surface tension are evaluated using the predicted front position \mathbf{X}_f , i.e.,

$$\rho^{n+1} = \rho(\mathbf{X}_f^{n+1}); \quad \mu^{n+1} = \mu(\mathbf{X}_f^{n+1}); \quad \mathbf{f}_b^{n+1} = \mathbf{f}_b(\mathbf{X}_f^{n+1}) \quad (22)$$

The velocity and pressure fields at new physical time level ($n+1$) are then computed by solving the flow equations by the FV method for a single physical time step, and finally the positions of the front points are corrected as

$$\mathbf{X}_f^{n+1} = \mathbf{X}_f^n + \frac{\Delta t}{2} (\mathbf{V}_f^n + \mathbf{V}_f^{n+1}) \quad (23)$$

After this step, the material properties and the body forces are also reevaluated using the corrected front position. Cubic B-splines are used for all the interpolations from the fixed curvilinear grid onto front points and from the front points onto fixed curvilinear grid, and for distributing surface tension onto fixed curvilinear grid. The overall method is second-order accurate both in time and space. It is emphasized that the method is implicit in physical time and the physical time step Δt is solely determined by accuracy considerations.

An auxiliary regular Cartesian grid is utilized for tracking the positions of the front points in the curvilinear grid and is found to be very robust and efficient. Details of the tracking algorithm can also be found in Muradoglu and Kayaalp [10]. The auxiliary regular Cartesian grid is also used to determine the material properties using the procedure developed by Unverdi and Tryggvason [8], which involves solution of a Poisson equation. Bilinear interpolations are used to interpolate the material properties from the regular grid onto the curvilinear grid. The front marker points are reflected back into the computational domain in the case that the points cross the solid boundary due to numerical errors. The surface tension is distributed only onto the neighboring grid points when the front is close to the solid boundary and care is taken to make sure that the distributed forces are equivalent to the surface tension. However, no special treatment is done when two fronts come close to each other in the computational domain.

We note that, in addition to the preconditioning method, a multigrid method similar to that of Caughey [9] and a local time-stepping method are used to further accelerate convergence rate in pseudotime stepping. The details of the FV method can be found in Muradoglu and Kayaalp [10].

4 Results and Discussion

The method is first validated for the test case of a buoyancy-driven drop rising in a straight channel, and the results obtained with the present method and with the well-tested FD/FT method of Unverdi and Tryggvason [8] implemented in the FTC2D code are compared. Then the method is applied to more challenging test cases of the buoyancy-driven drops in various constricted channels. Although the method is general and can handle many drop

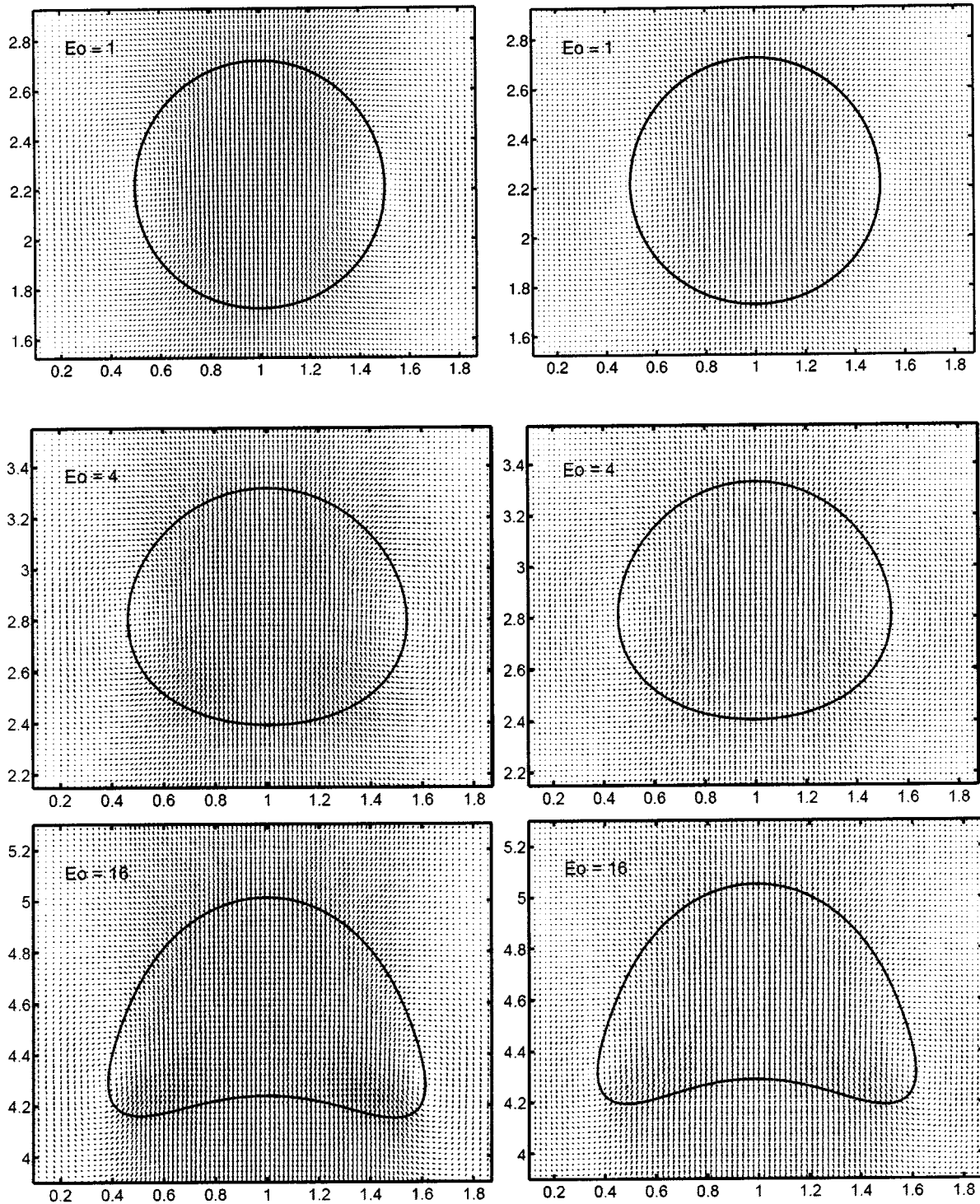


Fig. 1 Velocity vectors around a light drop rising in a straight channel for Eötvös and Morton numbers $Eo=1$, $M=10^{-4}$ (top plots), $Eo=4$, $M=4 \times 10^{-4}$ (middle plots) and $Eo=16$, $M=16 \times 10^{-4}$ (bottom plots) at $t^*=9.487$. Present results (left plots) are compared with the FTC2D results (right plot). Grid: 96×384 , $dt^*=0.0316$.

interactions, here only a single drop and two drop cases are considered. The computational results are expressed in terms of non-dimensional quantities. For this purpose, the length, time, and velocity scales are defined as $L=d_e$, $T=\sqrt{d_e/g}$ and $V_r = \mu_o/\rho_o d_e$, respectively, and the nondimensional quantities are denoted by*. For example, the x and y coordinates are nondimensionalized as $x^*=x/L$ and $y^*=y/L$, respectively. Although a three orders-of-magnitude reduction in the *rms* residuals of the

subiterations is found to produce essentially the same results; the *rms* residuals are reduced by four orders of magnitude in each inner iteration in pseudotime for all the simulations presented in this paper.

4.1 Freely Rising Drop in a Straight Channel. The method is first applied to a two-dimensional freely rising drop in a straight channel. The purpose of this test case is to validate the

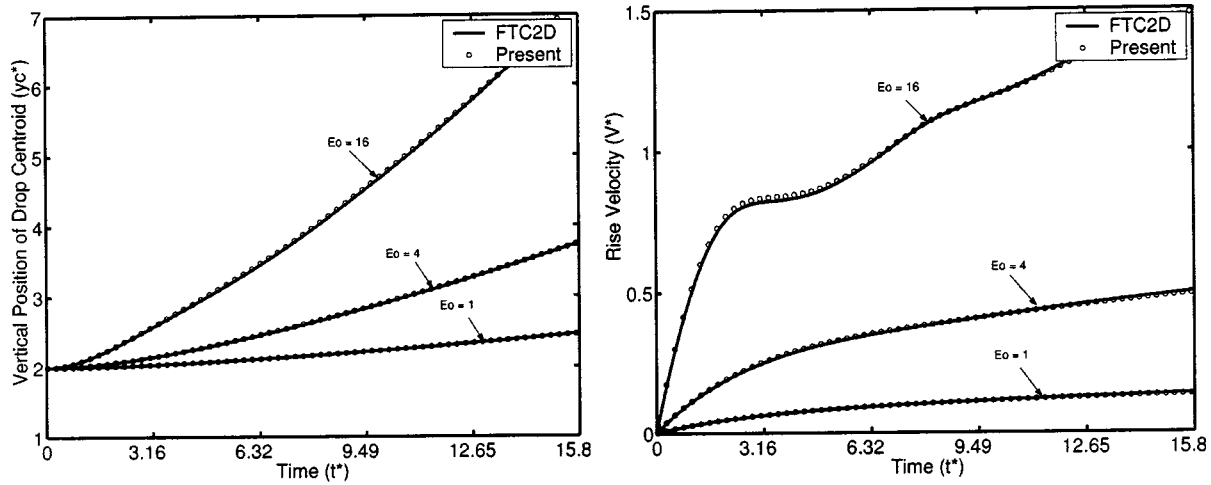


Fig. 2 The vertical positions (left plot) and the rise velocities (right plot) of the drop centroid taken from the simulations of the light drop rising in a straight channel. Computations are performed for Eötvös numbers 1, 4, and 16. The solid lines denote the FTC2D results and the symbols are the present calculations. Grid: 96×384 , $dt^* = 0.0316$.

method against the FD/FT method implemented in FTC2D code of Unverdi and Tryggvason [8] that can only use regular Cartesian grids. The computational domain is $2d_e \times 8d_e$, where d_e is the initial drop diameter and is resolved by a 96×384 uniform regular Cartesian grid. No-slip boundary conditions are applied on the side walls (i.e., $x=0$ and $x=2d_e$), while periodic boundary conditions are used in the vertical direction. The drop is initially an infinitely long circular cylinder centered at $(x_c^*, y_c^*) = (1.0, 2.0)$ and starts rising from the rest due to buoyancy forces at time $t^* = 0$. Freely rising drops take various shapes depending essentially on the Eötvös number.

To show this effect, computations are performed for three different Eötvös and Morton numbers (i.e., $Eo=1$, $M=10^{-4}$; $Eo=4$, $M=4 \times 10^{-4}$; and $Eo=16$, $M=16 \times 10^{-4}$), while the viscosity ratio is kept constant at $\zeta=1$. The corresponding density ratios are $\gamma=0.975$, 0.9 , and 0.6 , respectively. The physical time step is fixed at $dt^*=0.0316$, and the residuals are reduced by four orders of magnitude in each inner iteration in pseudotime. The drop shapes and the velocity vector field in the vicinity of the drop are plotted in Fig. 1 at time $t^*=9.487$ for the cases of $Eo=1$ (top plots), $Eo=4$ (middle plots), and $Eo=16$ (bottom plots). The results obtained with the FTC2D code are also shown in the right plots of Fig. 1. It can be seen in this figure that the present results are in good agreement with the FTC2D results demonstrating the accuracy of the present method. It is also observed that drop deformation increases as the Eötvös number increases as expected. To better quantify the accuracy of the present method the vertical position of the drop centroid and the drop rise velocity computed with the present method as well as with the FTC2D code are plotted as a function of time in Fig. 2. As can be seen in this figure, the present results are overall in very good agreement with the results of the FTC2D code except for the small discrepancies observed between the two results for $Eo=16$, which is partly attributed to the time-stepping error in the present results. Note that the time step used in the present method is about 20 times larger than that used in the FTC2D code for the case of $Eo=16$. Although the flow is incompressible, drop volume (area) changes due to numerical errors and the percentage change in the drop volume is a good indicator for the accuracy of the method. Figure 3 shows the percentage change of the drop area obtained with the present method and the FTC2D code for all three sets of dimensionless numbers. It can be observed in this figure that, in contrast with the FTC2D results, the drop volume reduces in time as the drop rises in the present method for this test case, but the overall percentage change in the drop volume is comparable in

magnitude in both methods. In summary the present results compare well with the results of the well-tested FD/FT method of Unverdi and Tryggvason [8] demonstrating the accuracy of the present algorithm.

4.2 Freely Rising Drops in Various Constricted Channels.

After validating the method for the case of a freely rising drop in a straight channel, we now consider buoyancy-driven drops rising in various constricted channels to show the ability of the method for treating dispersed multiphase flows in complex geometries where the phases strongly interact with the solid boundaries. The first test case concerns a single initially cylindrical drop rising due to buoyancy in a constricted channel. The channel is $2d_e$ wide, extends to $12d_e$ in the y direction, and is constricted sinusoidally at the middle by 75% as shown in Fig. 4(b). In Fig. 4(a), a portion of a coarse grid containing 32×192 grid cells is plotted in the vicinity of the constriction to show the overall structure of the body-fitted curvilinear grid used in the simulations. The governing nondimensional numbers are set to $Eo=8$, $M=8 \times 10^{-4}$, $\gamma=0.8$, and $\zeta=1$. No-slip boundary conditions are applied on the solid

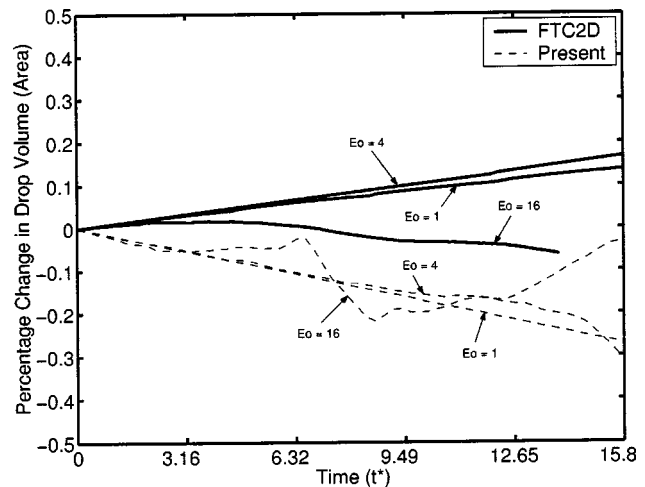


Fig. 3 Percentage change in the drop area for Eötvös numbers 1, 4, and 16 in the computations of the freely rising drop in the straight channel. Dashed curves denote the present results, and the solid curves are the FTC2D results. Grid: 96×384 , $dt^* = 0.0316$.

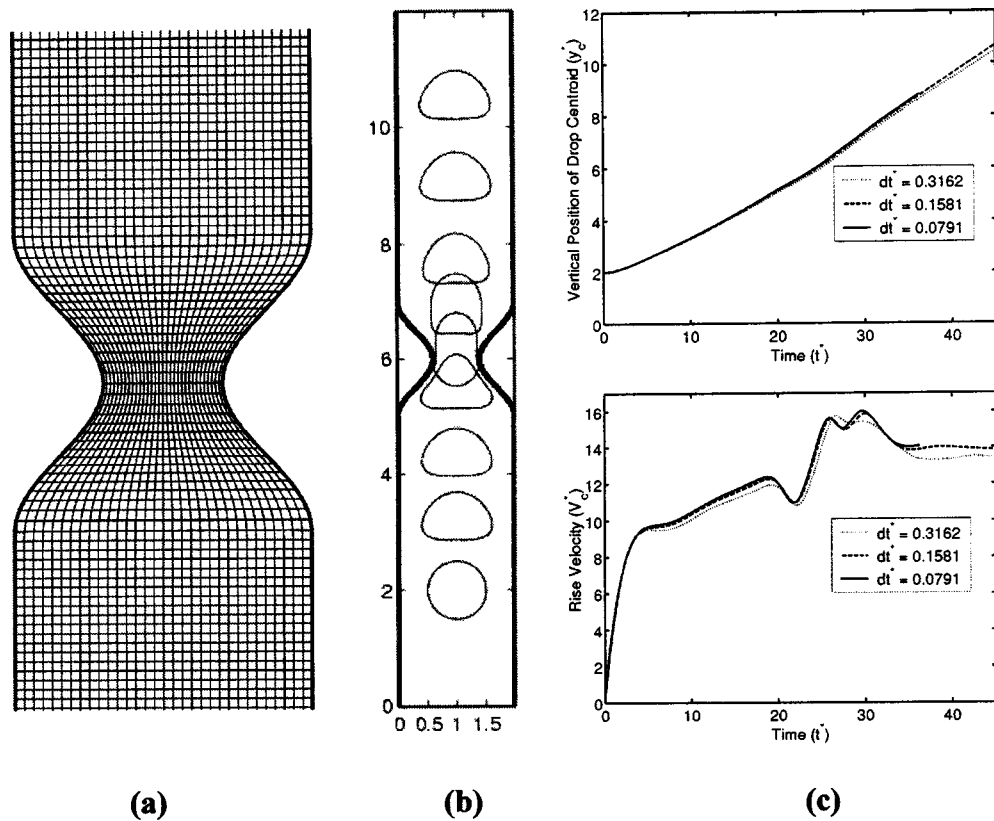


Fig. 4 Freely rising drop in a sinusoidally constricted channel. (a) A portion of the body-fitted curvilinear coarse grid containing 32×192 grid cells. (b) Snapshots taken at time frames $t^* = 0, 9.49, 15.81, 22.14, 28.46, 31.62, 37.95,$ and 44.27 . Time progresses from bottom to top. (c) The vertical position (top plot) and the rise velocity (bottom plot) of the drop centroid computed with the physical time steps $dt^* = 0.3162$ (dotted line), $dt^* = 0.1581$ (dashed line), and $dt^* = 0.0791$ (solid line). $Eu = 2, M = 8 \times 10^{-4}, \gamma = 0.8, \zeta = 1$. Grid: 128×768 .

walls, and periodic boundary conditions are employed in the vertical direction. The drop is initially centered at $(x_c^*, y_c^*) = (1.0, 2.0)$ and starts rising from the rest due to buoyancy forces. The snapshots taken at the time frames $t^* = 0, 9.49, 15.81, 22.14, 28.46, 31.62, 37.95,$ and 44.27 are plotted in Fig. 4(b) to show the overall behavior of the drop. The computations are performed on

a 128×768 grid. In order to better quantify the drop motion, the vertical position and the rise velocity of the drop centroid are plotted in Fig. 4(c). Computations are repeated for three different physical time steps (i.e., $dt^* = 0.3162, 0.1581,$ and 0.0791) on the same 128×768 grid to demonstrate the time-stepping error convergence. The small differences between the results computed

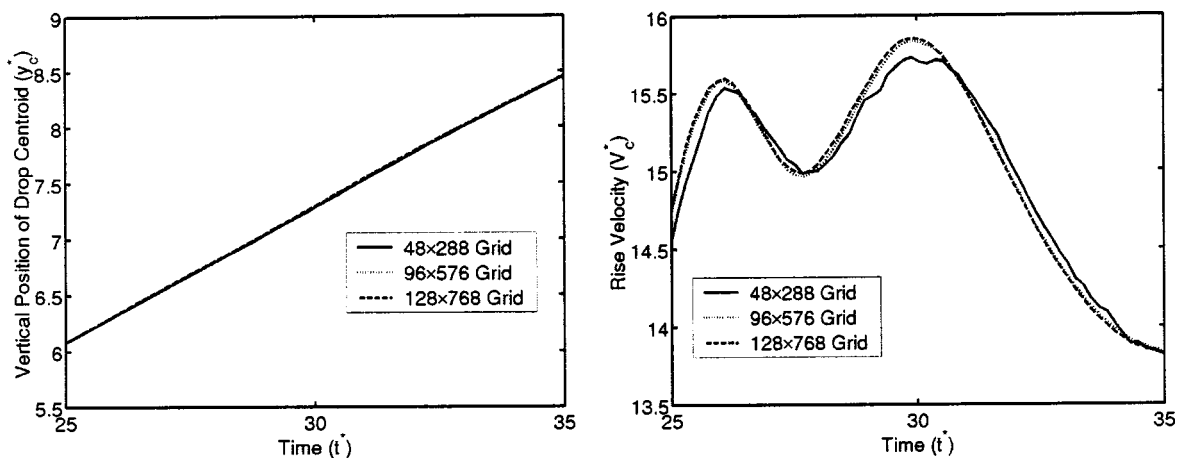


Fig. 5 Grid convergence analysis for the freely rising drop in the straight channel. The vertical position (left plot) and the rise velocity (right plot) of the drop centroid as a function of time computed on the body-fitted curvilinear grids containing 48×288 (solid line), 96×576 (dotted line) and 128×768 (dashed line) grid cells in the time interval $t^* = 25$ and $t^* = 35$. $dt^* = 0.1581, Eu = 4$.

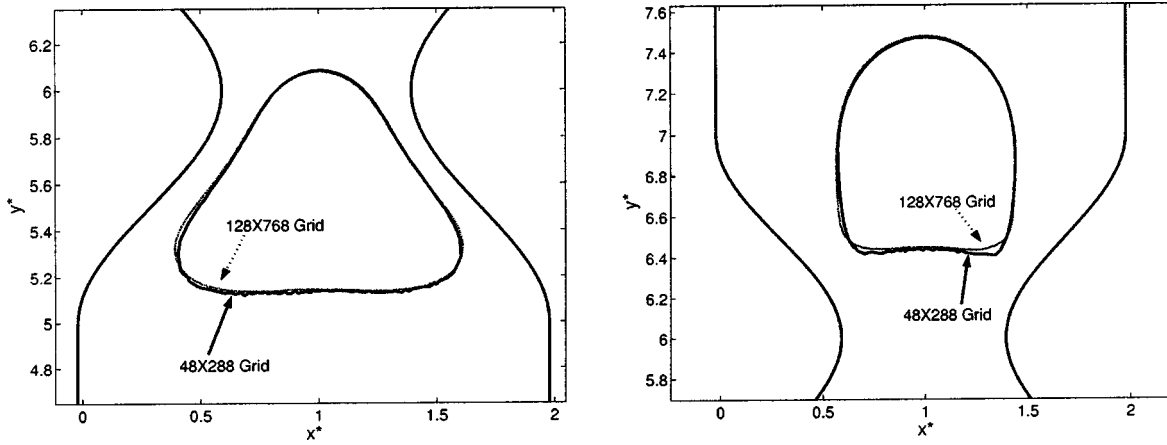


Fig. 6 Effects of grid refinement of the front structure. Before the drop enters (left plot, time $t^*=12.65$) and after it passes (right plot, time $t^*=22.14$) the constriction computed on 48×288 (solid line) and 128×768 (dashed line) grids. $dt^*=0.1581$, $Eu=4$. The coarse grid results in wiggles on the front while the front remains smooth in the case of the fine grid.

with the two smallest physical time steps indicate that the time-stepping error convergence is achieved and $dt^*=0.1581$ is sufficient for this test problem. Figures 4(b) and 4(c) together show that the drop motion initially resembles that of the straight-channel case before the drop starts feeling the effects of the con-

striction (i.e., before about $t^*=15$), but then it is strongly affected by the presence of the constriction as the drop passes through the constriction. In Fig. 5, the vertical position and the rise velocity of the drop centroid computed on 48×288 , 96×576 , and 128×768 grids are plotted to show the grid convergence. The physical time

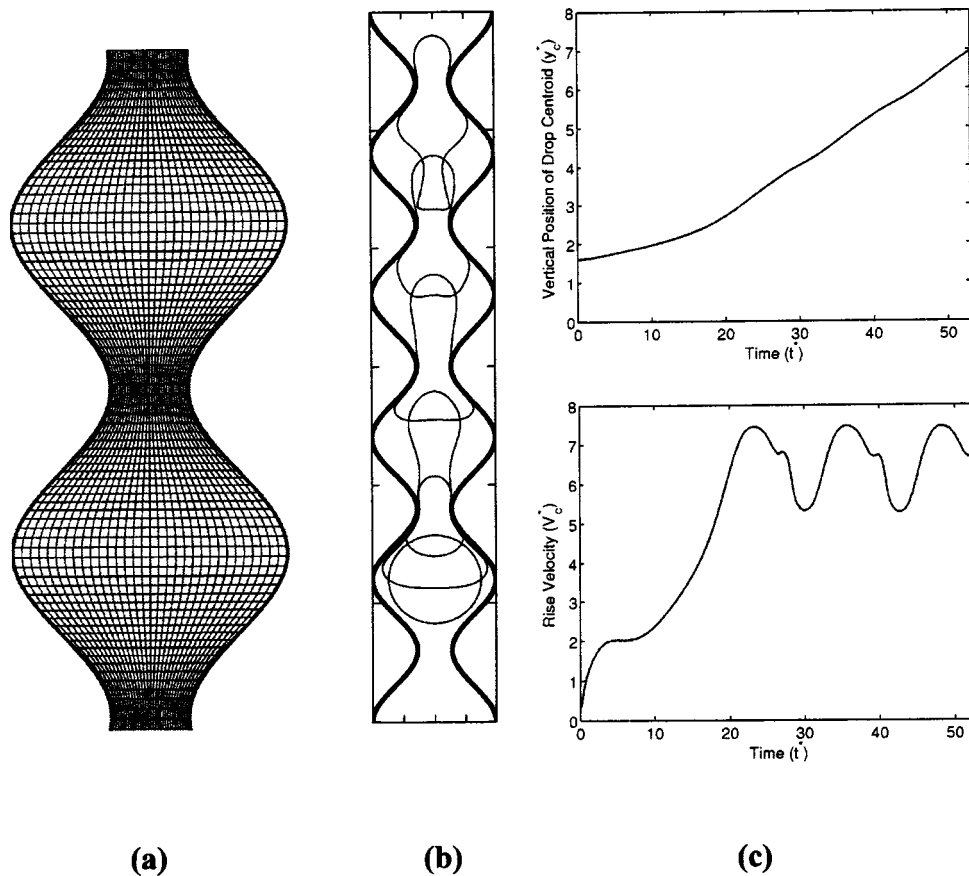


Fig. 7 Freely rising drop in a continuously constricted channel. (a) A portion of the body-fitted curvilinear coarse grid containing 32×192 grid cells. (b) Snapshots taken at time frames $t^*=0, 10.33, 20.66, 30.98, 41.31, \text{ and } 51.64$. Time progresses from bottom to top. (c) The vertical position (top plot) and the rise velocity (bottom plot) of the drop centroid computed with the physical time step $dt^*=0.1291$ on a 128×768 grid. $Eu=18$, $M=8 \times 10^{-4}$, $\gamma=0.8$, $\zeta=1$.

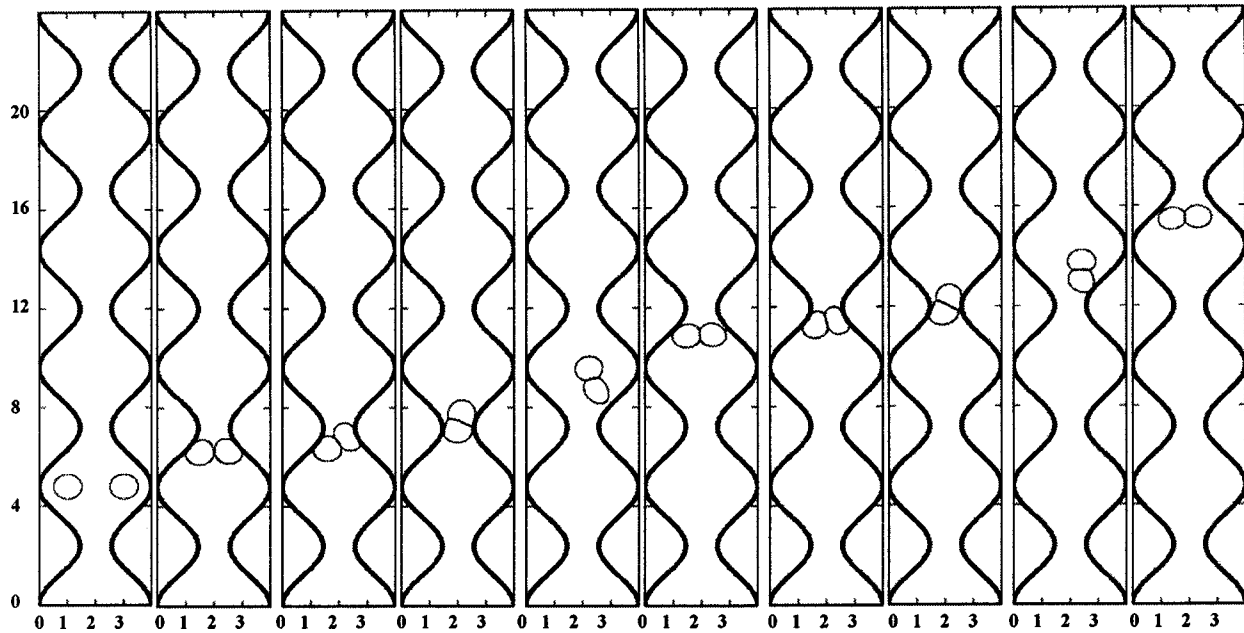


Fig. 8 Buoyancy-driven two-drop interaction in the continuously constricted channel. Snapshots taken at $t^*=0, 35.78, 53.67, 71.55, 89.44, 107.33, 125.22, 143.11, 161.00,$ and 178.89 . $Eu=2, M=8 \times 10^{-4}, \gamma=0.8$ and $\zeta=1$. Grid: 96×576 , $dt^*=0.2236$.

step is kept constant at $dt^*=0.1581$, and the results are shown only in the time interval $t^*=25$ and $t^*=35$, during which the drop passes through the constriction. The decreasing differences between results obtained on the successively finer grids indicate that the grid convergence is achieved and the 96×576 grid is sufficient for this test case. Figure 6 shows the fronts computed on the 48×288 and 128×768 grids just before the drop enters and after it passes the constriction in order to demonstrate the effects of the grid refinement on the front structure. As can be seen in this figure, the coarse grid results in wiggles on the front while the front remains very smooth in the case of the fine grid. Note that results obtained on the 96×576 grid is not plotted because it is almost indistinguishable from the 128×768 grid case.

The next test case concerns a buoyancy-driven drop freely rising in a continuously constricted channel depicted in Fig. 7(b).

The channel is $4d_e/3$ wide, and extends to $8d_e$ in the y direction, and is constricted along the y -axis by sinusoidal wavy walls. The constriction ratio is 75% as in the singly constricted channel case. The initial and the boundary conditions are the same as the singly constricted channel case, and the drop is initially centered at $(x_c^*, y_c^*) = (0.6667, 1.6)$. The governing nondimensional numbers are $Eu=18, M=8 \times 10^{-4}, \gamma=0.8,$ and $\zeta=1$. Computations are performed on a 96×576 grid with the constant physical time step $dt^*=0.1291$. A portion of a coarser grid containing 32×192 grid cells is plotted in Fig. 7(a). Note that a similar geometry was used by Hemmat and Borhan [2] in their experimental study of the buoyancy-driven drops and bubbles. The snapshots taken at the time frames $t^*=0.0, 10.33, 20.66, 30.98, 41.31,$ and 51.64 are plotted in Fig. 7(b) to show the overall evolution of the drop motion. The strong interactions between the drop and the solid

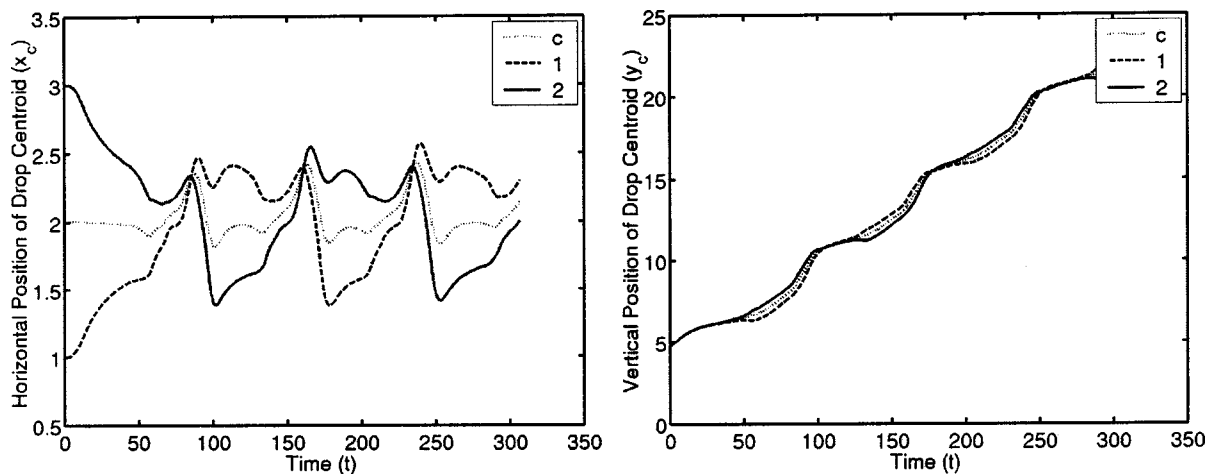


Fig. 9 Buoyancy-driven two-drop interaction in the continuously constricted channel. The horizontal (left plot) and the vertical (right plot) positions of the (initially) left drop centroid (solid line), the (initially) right drop (dashed line), and the center of the mass of the drop system (dotted line). $Eu=2, M=8 \times 10^{-4}, \gamma=0.8, \zeta=1$. Grid: 96×576 , $dt^*=0.2236$.

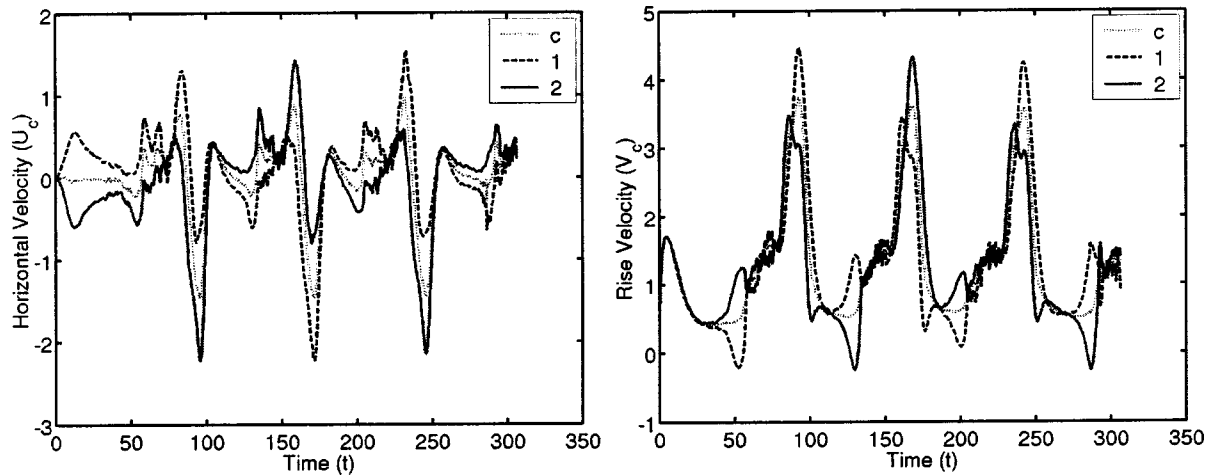


Fig. 10 Buoyancy-driven two-drop interaction in the continuously constricted channel. The horizontal (left plot) and the vertical (right plot) velocities of the (initially) left drop centroid (solid line), the (initially) right drop (dashed line), and the center of the mass of the drop system (dotted line). $Eo=2$, $M=8 \times 10^{-4}$, $\gamma=0.8$, $\zeta=1$. Grid: 96×576 , $dt^*=0.2236$.

walls can be clearly seen in this figure. It is emphasized that, in spite of large deformations, the front remains smooth, which might be considered as a good indication for the accuracy of the simulation. The vertical position and the rise velocity of the drop centroid are plotted in Fig. 7(c). It can be seen in this figure that the rise velocity becomes periodic after a transient period (i.e., after about $t^*=20$).

Finally, the method is used to compute two identical drops freely rising in the continuously constricted channel. In this case, the drop diameters are relatively small compared to the channel width, and the ratio of the initial drop diameter to the maximum channel width is $d_e/d_{\max}=0.25$. The corresponding nondimensional numbers are $Eo=2$, $M=8 \times 10^{-4}$, $\gamma=0.8$, and $\zeta=1$. The same 96×576 grid is employed as used in the single-drop case and the physical time step is taken as $dt^*=0.2236$. The drops are initially located at $(x_c^*, y_c^*)=(1.0, 4.8)$ and $(x_c^*, y_c^*)=(3.0, 4.8)$. The snapshots taken at the time frames $t^*=0, 35.78, 53.67, 71.55, 89.44, 107.33, 125.22, 143.11, 161.00$, and 178.89 are plotted in Fig. 8 to show the overall behavior of the drops. The drops strongly interact with the solid walls as well as with themselves and deform considerably as they pass through the constrictions. It is interesting to observe that the drops initially rise side by side but the right drop passes the first constriction little earlier than the left drop and then the left drop catches up and passes the right drop. After that the drops switches their positions and this behavior is repeated periodically after each constriction. This behavior can also be seen in Figs. 9 and 10, where the horizontal and vertical locations, the horizontal and vertical (rise) velocities of the individual drop centroids, and the center of the mass of the drop system are plotted. Note that neither breakup nor coalescence is allowed in the present simulations. It can be seen from these figures that the motion of a two-drop system becomes periodic after a transient period. Due to relatively poor grid resolution and large physical time step, drops lose about 20% volume when they move about 14 drop diameters (which corresponds to $t^*=215$). In spite of very strong interactions between the drops and the solid walls as well as between drops themselves and a relatively coarse grid, the periodic behavior of the two-drop system observed in

Figs. 9 and 10 indicates that the main features of the two-drop interactions are well captured by the present method.

5 Conclusions

The computations of buoyant drops in constricted channels have been reported in this paper. The FV/FT method is first validated for the case of a buoyancy-driven drop in a straight channel by comparing the results with the computations obtained by the well-tested FD/FT method implemented in FTC2D code [8]. The method has been successfully applied to buoyant drops in various constricted channels. Some error convergence studies have also been performed. It is found that the present method is a viable tool to model dispersed multiphase flows in arbitrarily complex geometries.

References

- [1] Olbricht, W. L., and Leal, L. G., 1983, "The Creeping Motion of Immiscible Drops Through a Diverging/Converging Tube," *J. Fluid Mech.*, **134**, 329–355.
- [2] Hemmat, M., and Borhan, A., 1996, "Buoyancy-Driven Motion and Deformation of Drops and Bubbles in a Periodically Constricted Capillary," *Chem. Eng. Commun.*, **148–150**, 363–384.
- [3] Udaykumar, H. S., Kan, H.-C., Shyy, W., and Tran-Son-Tay, R., 1997, "Multiphase Dynamics in Arbitrary Geometries on Fixed Cartesian Grids," *J. Comput. Phys.*, **137**, 366–405.
- [4] Tryggvason, G., Bunner, B., Esmaeeli, A., Juric, D., Al-Rawahi, N., Tauber, W., Han, J., Nas, S., and Jan, Y.-J., 2001, "A Front Tracking Method for the Computations of Multiphase Flows," *J. Comput. Phys.*, **169**, 708–759.
- [5] Tsai, T. M., and Miksis, J. M., 1994, "Dynamics of a Drop in a Constricted Capillary Tube," *J. Fluid Mech.*, **274**, 197–217.
- [6] Manga, M., 1996, "Dynamics of Drops in Branched Tubes," *J. Fluid Mech.*, **315**, 105–117.
- [7] Olbricht, W. L., and Kung, D. M., 1992, "The Deformation and Breakup of Liquid Drops in Low Reynolds Number Flows Through Capillaries," *Phys. Fluids*, **4**, 1347–1354.
- [8] Unverdi, S. O., and Tryggvason, G., 1992, "A Front-Tracking Method for Viscous, Incompressible Flows," *J. Comput. Phys.*, **100**, 25–37.
- [9] Caughey, D. A., 2001, "Unsteady Flows Past Cylinders of Square Cross-Section," *Comput. Fluids*, **30**, 939–960.
- [10] Muradoglu, M., and Kayaalp, A. D., 2004, "A Finite Volume/Front-Tracking Method for Computations of Dispersed Multiphase Flows in Complex Geometries" *J. Comput. Phys.* (submitted for publication).
- [11] Clift, R., Grace, J. R., and Weber, M. E., 1978, *Bubbles, Drops, and Particles*, Academic Press, San Diego, CA.